Probing Thermal Magnon Current Mediated by Coherent Magnon via Nitrogen-Vacancy Centers in Diamond

Dwi Prananto,[1,*,‡] Yuta Kainuma,[1] Kunitaka Hayashi,[1] Norikazu Mizuochi,[2] Ken-ichi Uchida,[3,4,5] and Toshu An[1,†]

[1] *School of Materials Science, Japan Advanced Institute of Science and Technology, Nomi, Ishikawa 923-1292, Japan*

[2] *Institute for Chemical Research, Kyoto University, Gokasho, Uji, Kyoto 611-0011, Japan*

[3] *National Institute for Materials Science, Tsukuba 305-0047, Japan*

[4] *Institute for Materials Research, Tohoku University, Sendai 980-8577, Japan*

[5] *Center for Spintronics Research Network, Tohoku University, Sendai 980-8577, Japan*

(Received 31 May 2021; revised 14 August 2021; accepted 24 November 2021; published 23 December 2021)

Currently, thermally excited magnons are being intensively investigated, owing to their potential in computing devices and thermoelectric conversion technologies. We report the detection of a thermal magnon current propagating in a magnetic insulator yttrium iron garnet under a temperature gradient using a quantum sensor: electron spins associated with nitrogen-vacancy (N-V) centers in diamond. A thermal magnon current is observed as modified Rabi-oscillation frequencies of N-V spins hosted in a beam-shaped bulk diamond that is resonantly coupled with coherent magnon propagating over a long distance. Additionally, using a nanodiamond, alteration in N-V spin-relaxation rates, depending on the applied temperature gradient, are observed under nonresonant N-V excitation conditions. The demonstration of probing a thermal magnon current mediated by coherent magnons via N-V spin states serves as a basis for creating a device platform that hybridizes spin caloritronics and spin qubits.

DOI: 10.1103/PhysRevApplied.16.064058

I. INTRODUCTION

The utilization of magnons, i.e., the quanta of collective spin excitation, in magnetic media for transmitting and processing information has flourished in the last decade and is known as magnon spintronics [1–4]. Moreover, the emerging field of spin caloritronics [5], which utilizes the interplay between spin and heat currents, results in an alternative strategy for creating more efficient computing devices [6,7] and versatile thermoelectric conversion technologies [8]. Progress in the magnon-spintronics and spin-caloritronics field benefits from the ubiquitous use of spin-transport measurements based on the inverse spin Hall effect (ISHE) [9], in which a paramagnetic heavy metal is patterned on a ferromagnetic medium [2,6,8].

Quantum sensors based on electron spins in diamond with nitrogen-vacancy (N-V) centers are regarded as eminent sensors for various condensed matter phenomena [10–12], including spin waves, as they offer high spatial resolution at the nanoscale, enabling fluctuating magnetic fields with a broad frequency band from static to GHz and nonperturbative operation [10,13] to be probed. N-V centers are well coupled to coherent magnetostatic spin waves (MSWs), owing to their energy matching [14–20]. Recently, magnon population has been measured and controlled via pumping the N-V center by spin waves with a single N-V spin sensitivity [21–23]. Furthermore, the same effect is observed nonlocally using the ISHE [24]. Additionally, N-V spin excitations and modulations via the spin-transfer-torque oscillation of spin waves by electrical methods through the spin Hall effect have been demonstrated recently [25–27].

In contrast, thermally excited magnons with significantly higher energy [28] (defined by $\hbar\omega = k_B T$) than that of N-V spins cannot resonantly excite N-V spins, whereas the high-energy magnons can affect the N-V relaxation rate in a nonresonant way [29,30]. This high-energy magnon current is known to interact with lower-energy MSWs through the thermal magnon spin-transfer torque [31–36]. Thus, probing the thermal magnon current via N-V spins can be realized using MSWs as a mediator.

Herein, we report the detection of a thermally excited magnon current mediated by MSWs by exploiting the thermal magnon spin-transfer torque (Fig. 1), bridging the

*prananto@jaist.ac.jp

†toshuan@jaist.ac.jp

‡Present address: Materials Science Program, Faculty of Engineering, Niigata University, Niigata City, Niigata 950-2181, Japan.

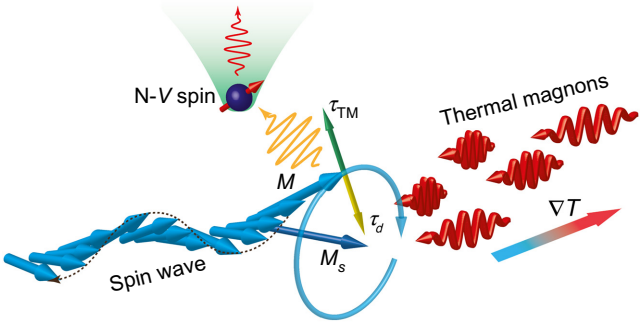

FIG. 1. Mechanism of thermal magnon current detection via N-V center. In a magnet, thermal magnon current is created by applying temperature gradient ∇T, exerting torque τ_{TM} (with damping torque τ_d) to spin wave's (coherent magnon) precessing magnetization M excited by a microwave ac field. Then, information on thermal magnon current can be probed by N-V center's spin in diamond near the magnet through the spin wave.

energy gap between the thermally excited magnons and N-V spins. Using an ensemble of N-V spins in bulk diamond, we observe the modification of the magnetostatic surface spin waves' (MSSWs') magnetization dynamics under resonant N-V-spin excitations influenced by the thermal magnon current in a magnetic insulator, yttrium iron garnet (YIG). Additionally, under nonresonant N-V-spin excitation conditions in a nanodiamond, we also observe N-V relaxation-rate changes related to the thermal magnon current.

II. METHODS

We use a liquid-phase-epitaxy-grown YIG sample in the form of a trilayer of single-crystalline YIG-gadolinium gallium garnet (GGG)-YIG of thicknesses 100, 550, and 100 μm, measuring 6×3 mm^2 [Fig. 2(a)]. To improve lattice matching between YIG and GGG, a small amount of yttrium in the YIG is substituted with bismuth.

Throughout the experiments, external magnetic fields, $\pm B_{\text{ext}}$, are applied along the y axis with a tilted angle, ϕ, to the surface plane of YIG/GGG/YIG [Fig. 2(a)]. Two gold-wire antennas A and B (50 μm in diameter) are overlaid on the surface near both edges of the upper YIG, approximately 2 mm away, for excitation of MSSWs by an electrical microwave field, and the MSSWs propagate along the $k \parallel B_{\text{ext}} \times \hat{\mathbf{n}}$ direction ($\hat{\mathbf{n}}$ is a vector normal to the YIG's surface) [37]. In this setup, the MSSWs are predominantly excited on the upper YIG layer's surface by one of the antennas and propagate to the other end of the sample, depending on the polarity of the applied external magnetic field, where $+B_{\text{ext}}$ ($-B_{\text{ext}}$) is along the $+y$ ($-y$) axis [Fig. 2(a) shows the case for excitation of antenna A].

We use two types of diamond N-V centers: a diamond beam [(110)-oriented] measuring $2.5 \times 0.1 \times 0.1$ mm^3, containing a layer of the N-V spin ensemble (occupying a depth up to 70 nm and a mean depth of 40 nm beneath the surface, see Supplemental Material Note 1 [38]), and a nanodiamond with a diameter of approximately 40 nm, containing several N-V spins (Adámas Nanotechnologies). It is noteworthy to mention that the use of the diamond beam with a well-known N-V axis direction is suitable for efficient resonant N-V spin excitations but not for nonresonant excitations, owing to the significant distance of approximately 1 μm separating the N-V spins and the YIG surface [20,39]. As shown in Fig. 2(a), the diamond beam is placed on the upper YIG layer at the middle of its longitudinal direction, where an external magnetic field, $+B_{\text{ext}}$, directed along the y axis ([00$\bar{1}$] crystal direction of the diamond beam) creates an angle, ϕ, of 32° to the (110) plane [157° to N-V3 ($\parallel$ [111])] of the diamond beam [Fig. 2(a)]. This setup separates the resonance transitions of four possible N-V spins directing to the $\langle 111 \rangle$-symmetrical axes (N-V1 $\parallel[1\bar{1}\bar{1}]$, N-$V$2 $\parallel[\bar{1}1\bar{1}]$, N-$V$3 $\parallel$[111], and N-V4 $\parallel[\bar{1}\bar{1}1]$).

A temperature gradient, ∇T , is created along the YIG's longitudinal direction by increasing or lowering the temperature at either site A (T_A) or site B (T_B). Such temperature control keeps the temperature at the middle of the YIG's longitudinal dimension constant, as well as the diamond beam's temperature, under the application of temperature differences, ΔT, up to 10 K [Fig. 2(a)]. This is confirmed using the temperature-sensing capability of the N-V spins [40–42] and infrared thermography (see Supplemental Material Notes 4 and 5 [38]). ΔT is defined as the difference between T_A and T_B ($\Delta T = T_A - T_B$).

For the optically detected magnetic resonance (ODMR) measurements, the N-V spins' ground triplet ($^3A_2$) states, $m_s = 0$ and $m_s = \pm 1$, are optically addressed using an in-house scanning confocal microscope (see Supplemental Material Note 2 [38]). In this study, spin-state manipulation, $m_s = 0 \leftrightarrow \pm 1$, is performed by using MSSW-generated electromagnetic microwave radiation [Fig. 2(b)], propagating from one of the gold-wire antennas to the laser-spot position separated by approximately 1 mm [17,18].

III. RESULTS

A. Spin-wave and N-V spin-resonance mapping

The MSSWs are excited from antenna A with microwave (MW) power $P_{\text{MW}} = 1$ mW, in an increasing $+B_{\text{ext}}$, and the YIG's global coherent spin-wave resonance spectra are mapped out by performing microwave-absorption (S_{11} parameter) measurements using a vector network analyzer (Rohde & Schwartz ZVB8) at $\Delta T = 0$. Figure 2(c) shows a map of the spin-wave spectra, exhibiting lines of resonance of the MSSWs spanning to higher frequencies from the uniform Kittel mode [ferromagnetic resonance (FMR)]. The solid red and yellow lines indicate the N-V spins' upper ($m_s = 0 \leftrightarrow +1$) and lower

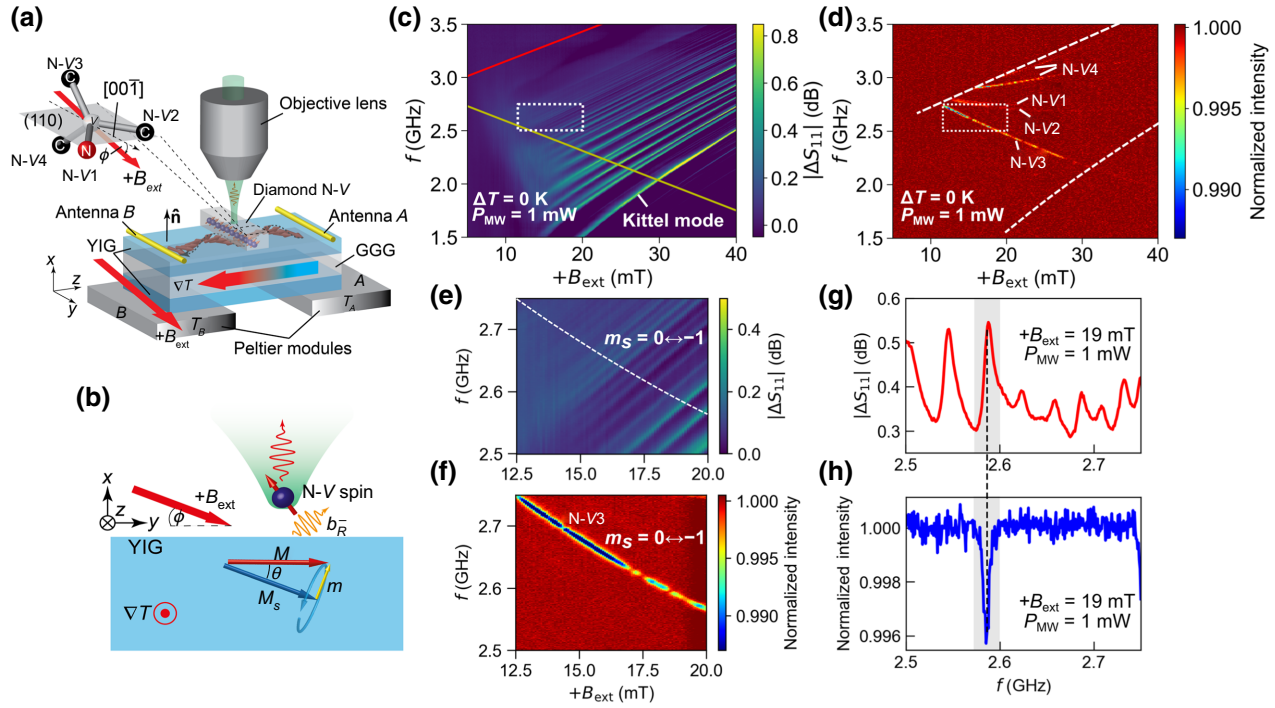

FIG. 2. Experimental setup with a diamond beam and mapping of spin waves and N-V spin-resonance spectra. (a) Experimental setup for probing thermally excited magnon current via N-V centers in a diamond beam centered on the upper YIG surface. (b) Schematic model of thermal magnon current spin-transfer torque system with N-V spin (dark blue ball with red arrow) and precessing magnetization M in YIG (red arrow) under magnetic field B_{ext}. Transverse component, m, of M produces ac magnetic field amplitude b_R^- that drives N-V spin into its Rabi oscillation. Thermal magnon spin-transfer torque produced by temperature gradient ∇T is exerted on M resulting in the modification of b_R^-. M_s is the saturation magnetization of the YIG. (c) Microwave absorption ($P_{\text{MW}} = 1$ mW) spin-wave resonance spectra as a function of externally applied magnetic field, $+B_{\text{ext}}$ [solid lines indicate upper (red, $m_s = 0 \leftrightarrow +1$) and lower (yellow, $m_s = 0 \leftrightarrow -1$) bounds of possible ground-state resonance transitions of N-V spins]. MSSWs are observed at higher frequencies above the Kittel mode (FMR). (d) ODMR spectra of N-V spins in the diamond beam as a function of $+B_{\text{ext}}$ field. Region between two dashed white lines indicates the resonance frequency band of MSSWs. N-V1 to N-V4 indicate four possible N-V spins directed to ⟨111⟩-symmetrical axes, as shown in (a). (e) Magnified spin-wave resonance spectra at white squares in (c). Dashed white line indicates resonance transitions of N-V3 spins in (d). (f) Magnified ODMR spectra of white squares in (d), showing discretized ODMR resonance line of N-V3, owing to crossing with MSSWs' resonant frequencies. (g) Line cut of (e) at $+B_{\text{ext}} = 19$ mT. (h) Line cut of (f) at $+B_{\text{ext}} = 19$ mT. (g),(h) Matching conditions at frequency of 2.58 GHz.

($m_s = 0 \leftrightarrow -1$) bound resonance transitions, respectively, defined by the Zeeman energy [18]. When an energy-matching condition between the MSSW and N-V spin is fulfilled ($f_{\text{MSW}} = f_{\text{N-}V}$), the N-$V$ spins can be coherently excited by the MSSWs [17,18]. From the results in Fig. 2(c), we can expect excitations of the N-V spins by the MSSWs within the red and yellow lines.

Next, we map out the MSSW-driven N-V spin-resonance frequencies by performing ODMR spectroscopy with an increasing $+B_{\text{ext}}$ at $\Delta T = 0$ using the diamond beam. Figure 2(d) shows a color map of the MSSW-driven ODMR in the diamond beam. As expected, only the N-V spin-resonance transitions that match with the MSSW resonance frequencies undergo PL-intensity quenching, as a consequence of the transition from $m_s = 0$ to $m_s = \pm 1$ [17,18]. In Fig. 2(d), only the $m_s = 0 \leftrightarrow -1$ transitions that overlap with the MSSW resonance frequencies appear. Furthermore, by magnifying the N-V3 spectral line in Fig. 2(d), a discretized and broadened resonance line, owing to frequency matching between the N-V spins and the MSSWs with different allowed-k wave numbers [Fig. 2(e)] is observed [Fig. 2(f)] [19,43]. The spectra at a matching condition with $+B_{\text{ext}} = 19$ mT and $f_{\text{MW}} = 2.58$ GHz between a MSSW with a specific wave number and the N-V spins are shown in Figs. 2(g) and 2(h).

B. Detection of thermal magnon current via coherent driving of N-V spins

In a magnet under a temperature gradient, a thermal magnon current is generated [4,8] and exerts a thermal spin-transfer torque, $\boldsymbol{\tau}_{\text{TM}}$, to a precessing magnetization of coherently excited MSSWs [Figs. 1 and 2(b)]. The phenomenon is well known to be detected through a microwave response [36] and the ISHE [33–35]. Here, an ensemble of N-V spins in a diamond beam is utilized to

detect the thermal magnon current mediated by MSSWs [Figs. 2(a) and 2(b)]. Notably, the applied magnetic field is perpendicular to MSSW propagation and the temperature-gradient direction [Fig. 2(a)], different from that of Yu *et al.*'s setup [36] (parallel). Within this geometry, the thermal magnon current is not detectable through the ISHE, since there is no measurable ISHE voltage along the paramagnetic heavy-metal stripe, if it is deposited parallel to spin-polarization vector $\boldsymbol{\sigma}$ along the lateral dimension of the YIG as $V_{\mathrm{ISHE}} \parallel J_s \times \boldsymbol{\sigma}$, where V_{ISHE} and J_s are the ISHE voltage and spin-current vector, respectively [9,34].

First, the ODMR spectra of the N-V spins excited by the MSSWs are analyzed under a temperature gradient. We tune the resonance frequency to one of the matching-condition frequencies of 2.58 GHz, as shown in Figs. 2(g) and 2(h) and analyze the PL contrast of the ODMR as ΔT is varied. In Fig. 3(a), the ODMR spectra, with a resonance dip at 2.58 GHz ($+B_{\mathrm{ext}} = 19$ mT, $P_{\mathrm{MW}} = 1$ mW), are shown with an increasing ΔT (-10 to $+10$ K). The ODMR's PL contrast is enhanced as ΔT evolves from positive to negative, although the MSSWs are driven by the same MW power, $P_{\mathrm{MW}} = 1$ mW. Their intensities are plotted together with linear fitting in Fig. 3(b). This indicates a change in the amplitude of the microwave ac field from the MSSWs [44], as a thermal magnon current is generated under the application of a temperature gradient in the upper layer of the YIG.

Next, we drive the N-V spins into the Rabi oscillations between $m_s = 0$ and $m_s = -1$ via the MSSW-driven pulse sequence shown in Fig. 3(c) with the same matching condition of 2.58 GHz between the qubit states of $m_s = 0$ and $m_s = -1$ [Fig. 3(d)]. The frequency of the Rabi oscillation, Ω_R^-, is proportional to the amplitude of the MSSW oscillating driving field, b_1 ($\Omega_R^- \propto b_1$). The negative-sign superscript denotes the left-handed polarization component of the oscillating field of the MSSWs driving the N-V spin transition ($m_s = 0 \leftrightarrow -1$) [20,45,46]. The Rabi frequency is enhanced for $\Delta T = 0$ to -10 K and is suppressed for $\Delta T = 0$ to $+10$ K [Figs. 3(d) and 3(e)]. This is explained by the change of polarity of the thermal magnon spin-transfer torque [36] (Fig. 1). The amplitude of the Rabi field, b_R^-, defined as an effective oscillating electromagnetic field acting at the N-V position above the YIG surface [Fig. 2(b)], can be estimated from the Rabi frequency through the relationship $b_R^- = \Omega_R^-/\gamma_e$ [14,45,46], with $\gamma_e = 2\pi \times 28$ GHz/T being the gyromagnetic ratio of electrons. The Rabi-field amplitude, b_R^-, evolves from (19 ± 0.5) μT at $\Delta T = 10$ K to (26 ± 0.4) μT at $\Delta T = -10$ K, based on its plot as a function of ΔT [Fig. 3(f)], indicating a change of approximately (18 ± 1)% from (22 ± 0.6) μT at $\Delta T = 0$.

The unidirectional propagation of MSSWs is inverted according to $k \parallel B_{\mathrm{ext}} \times \hat{\mathbf{n}}$ [47,48] by applying a different polarity of B_{ext} at the upper YIG surface, and under this condition, the thermal spin-transfer torque is applied with different polarity [36]. Hence, we can expect to observe the same but inverted sign effect when we switch the external magnetic field to the $-y$ axis (assigned as $-B_{\mathrm{ext}}$) and launch the MSSWs from antenna B [36]. We tune the N-V resonance frequency to a matching condition of 2.60 GHz ($-B_{\mathrm{ext}} = 19$ mT, $P_{\mathrm{MW}} = 1$ mW). As expected, the Rabi frequency is suppressed for $\Delta T = 0$ to -10 K and is enhanced for $\Delta T = 0$ to $+10$ K [Figs. 3(g) and 3(h)]. In this geometry, the Rabi-field amplitude is estimated to evolve from approximately (18 ± 0.6) μT at $\Delta T = -10$ K to approximately (22 ± 0.3) μT at $\Delta T = +10$ K [Fig. 3(i)], indicating a change of approximately (16 ± 2)% from (19 ± 0.5) μT at $\Delta T = 0$.

The observed effect can be interpreted as a thermal magnon spin-transfer torque, τ_{TM}, via the thermal magnon current generated by a temperature gradient [4,49,50], which interacts with the MSSW and relaxes by transferring its spin angular momentum (Fig. 1). The transfer of spin angular momentum contributes to the development of the thermal magnon torque, τ_{TM} , which alters the MSSW's magnetization dynamics [31,32,36] and is perceived by the N-V spins as an altering Rabi-field amplitude [Fig. 2(b) and see Supplemental Material Note 9 [38]]:

$$b_R^- \propto \lambda M_s \frac{\gamma_e b_{\mathrm{MW}}}{(\alpha_i + a\nabla T)\omega_r} k e^{-kx}, \tag{1}$$

where λ, M_s, b_{MW}, α_i, ω_r, and x are, respectively, the proportionality constant, the saturation magnetization of the YIG, the microwave field driving the MSSWs, the intrinsic damping parameter of the YIG, the resonance frequency of the MSSW, and the distance separating the N-V spin and magnetization precession. The contribution from thermal magnons can be quantified by the thermal magnon damping parameter, which is proportional to the temperature gradient, $\alpha_{\mathrm{TM}} = a\nabla T$ (see Supplemental Material Note 8 [38]). Using a constant, a, in Eq. (1) as a fitting parameter, α_{TM} is estimated to be $(10 \pm 0.9) \times 10^{-4}$ for $+B_{\mathrm{ext}}$ and $(4.3 \pm 1) \times 10^{-4}$ for $-B_{\mathrm{ext}}$ using an effective temperature difference of $\Delta T_{\mathrm{eff}} = 6.6$ K over 2-mm distance at the YIG's top surface under applied $\Delta T = 10$ K.

The thermal magnon damping parameter values agree well with those reported previously [33–36], confirming the existence and contribution of the thermal magnon current in the evolution of MSSW magnetization dynamics [26,31,32,36]. Furthermore, we confirm our observation of the thermally excited magnon current electrically by analyzing the spin-wave-resonance linewidth from the absorption microwave signal (S_{11}) (see Supplemental Material Note 7 for experimental details and data [38]).

C. Local detection and nonresonant N-V spin excitation

We extend the capability to detect the thermally excited magnon current locally and nonresonantly to

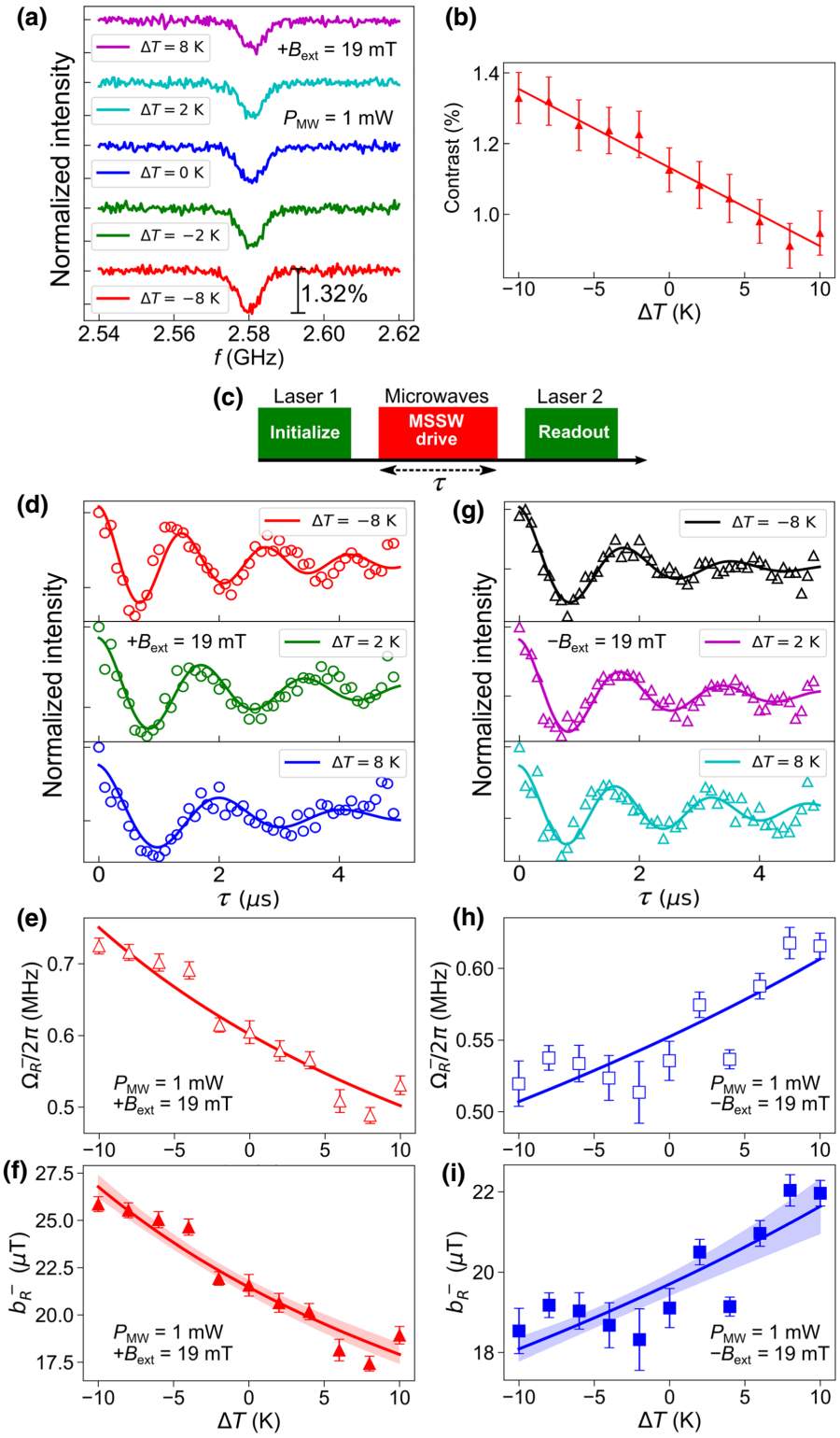

FIG. 3. ODMR spectra and Rabi-oscillation frequencies under temperature differences. (a) ODMR spectra with various temperature differences, ΔT, applied to the YIG at $+B_{\mathrm{ext}} = 19$ mT and $P_{\mathrm{MW}} = 1$ mW. ODMR dip contrast evolves monotonically (solid line) with ΔT applied to the YIG. (b) ODMR contrast as a function of ΔT applied to the YIG. Error bars are obtained from the standard-deviation error of curve fitting to data in (a) using a single Lorentzian function (not shown here). (c) Measurement protocol to excite Rabi oscillation on the N-V spins. Laser pulse 1 initializes the N-V spins to the $m_s = 0$ state followed by a microwaves pulse with duration τ that drives MSSWs in the YIG, which then excite N-V spins to the $m_s = -1$ state. Laser pulse 2 probes the remaining N-V spin population at the $m_s = 0$ state. τ is varied to produce a stroboscopic oscillation between $m_s = 0$ and $m_s = -1$ states. (d) Rabi oscillations at three different ΔT applied to the YIG for $+B_{\mathrm{ext}} = 19$ mT. Frequency of Rabi oscillation evolves with applied ΔT. Colored solid lines are damped sinusoidal functions. (e) Variation in Rabi-oscillation frequency, $\Omega_R^-/2\pi$, with ΔT. (f) Calculated Rabi-field amplitude, b_R^-, inferred from the Rabi frequency in (e) as a function of applied ΔT. (g)–(i) Rabi oscillations, Rabi frequencies, and Rabi-field amplitudes, respectively, as a function of ΔT with $-B_{\mathrm{ext}} = 19$ mT. Error bars in (e),(f),(h),(i) are obtained from the standard deviation of curve fitting to data in (d),(g), respectively, with a damped sinusoidal function. Colored solid lines in (e),(f),(h),(i) are fittings to Eq. (1). Shaded red and blue areas in (f),(i) are possible variations in fitting curves based on the uncertainties of fitting parameters in Eq. (1) (see Supplemental Material Note 10 [38]).

N-V spin-transition frequency via a small number of N-V spins in a nanodiamond [Fig. 4(a)]. The nanodiamonds with 40-nm average diameter are transferred to the middle of the YIG's longitudinal direction by dropping a small amount of nanodiamond solution with a micropipette.

With the same setup and technique as those used in experiments with a diamond beam, we map out the ODMR spectra of the N-V spins in a nanodiamond to obtain information regarding coupling between the long-distance propagating magnons and N-V spins. Figure 4(b) shows the magnon-driven ODMR spectral map, exhibiting PL

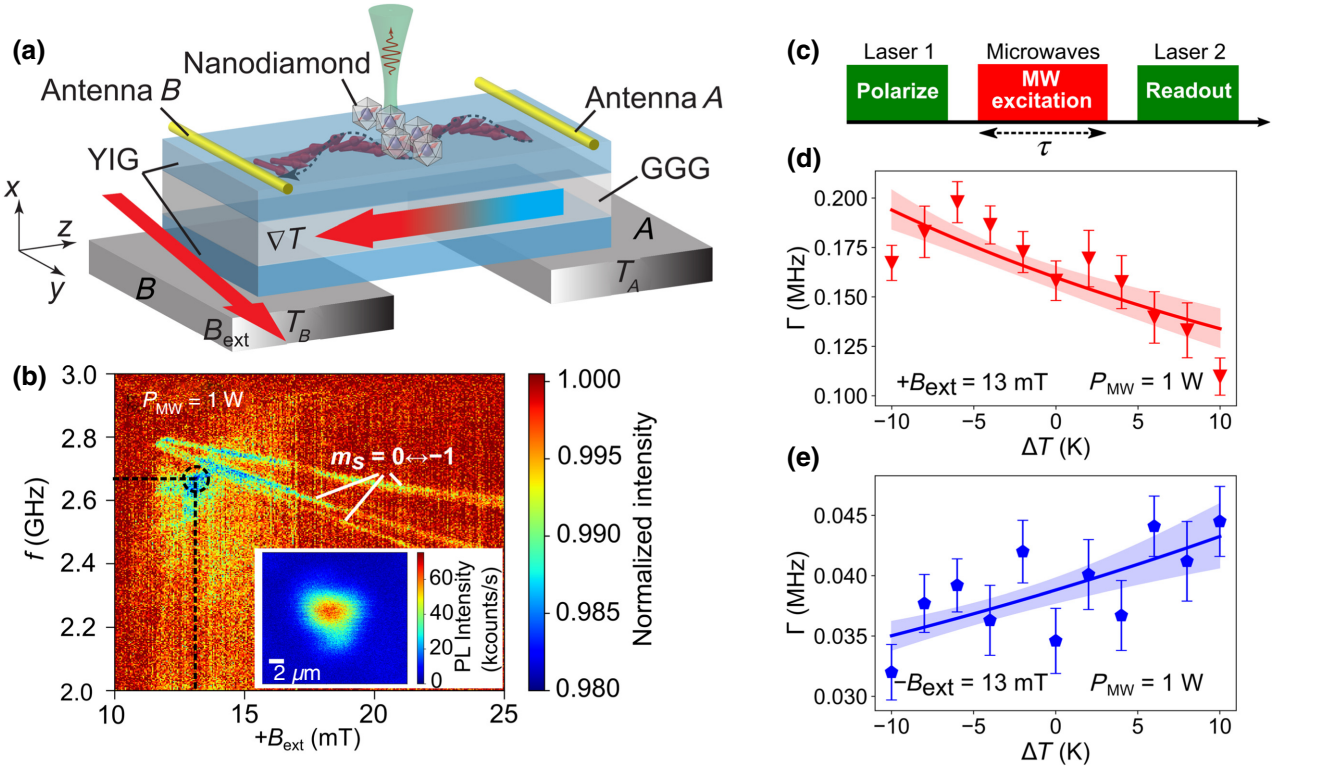

FIG. 4. Local detection of thermal magnon current using a nanodiamond. (a) Experimental setup for local detection of thermally excited magnon current with a nanodiamond containing several N-V spins. (b) ODMR spectral map of N-V spins in the nanocrystal diamond on the YIG under zero temperature difference, ΔT (P_{MW}= 1 mW). Nonresonant PL quenching is observed beside the straight lines of the N-V spin-resonant transitions, $m_s = 0 \leftrightarrow -1$. Inset shows a fluorescence image of the nanodiamond used in the measurement. (c) Longitudinal spin-relaxation-rate measurement protocol to detect the thermally excited magnon current, comprising of a polarizing laser pulse followed by a variable duration, τ, pulse of nonresonant N-V spin excitation via MSSWs at a frequency of 2.66 GHz with $\pm B_{ext} = 13$ mT [dashed black circle in (b)]. (d),(e) N-V spin-relaxation rate, Γ, as a function of ΔT applied to the YIG for $+B_{ext}$ [(d)] and $-B_{ext}$ [(e)]. Solid red line in (d) and blue line in (e) are fitting curves to data with a model in Eq. (2). Error bars in (d),(e) are obtained from the standard deviation of curve fitting to longitudinal spin-relaxation data with a single-exponential function (see Supplemental Material Note 6 [38]). Shaded red and blue areas in (d),(e) are possible variations in fitting curves based on uncertainties of fitting parameters in Eq. (2) (see Supplemental Material Note 10 [38]).

quenching at the resonance transition ($m_s = 0 \leftrightarrow -1$) of N-$V$ spins together with a PL image of the nanodiamond used in the measurements (inset) ($P_{MW} = 1$ W). Additionally, strong nonresonant PL quenching is observed away from the N-V spin transitions [15,39] at frequencies ranging from 2.5 to 2.7 GHz at $+B_{ext}$ between 11.5 and 13.5 mT [Fig. 4(b)], where MSSWs with higher-k wave numbers are within the range observed in Fig. 2(e).

Next, we perform longitudinal spin-relaxation measurements, in which N-V spins are polarized to $m_s = 0$ by the first laser pulse, followed by a dark time, τ, before another laser pulse is applied to read the remaining population [Fig. 4(c)]. By varying τ, the time-trace relaxation of the $m_s = 0$ state to its equilibrium state is observed. Under the application of ∇T to the YIG, a MW pulse with a frequency of 2.66 GHz and $+B_{ext}$ and $-B_{ext} = 13$ mT [marked by black circles in Fig. 4(b)] is applied with $P_{MW} = 1$ W during time τ.

Figures 4(d) and 4(e) show measurements of the longitudinal N-V spin-relaxation rate, Γ, as a function of applied temperature gradient with MW driven in the YIG under opposite polarity of external magnetic fields, $+B_{ext}$ and $-B_{ext}$. For $+B_{ext}$, the longitudinal relaxation rate increases for $\Delta T = 0$ to -10 K and decreases for $\Delta T = 0$ to $+10$ K [Fig. 4(d)]. Opposite polarity of the slope change of Γ is observed when the polarity of B_{ext} is inverted [Fig. 4(e)]; this is reasonable with respect to the MSSW's unidirectional propagation character.

Here, we assume that the observed effect originates from the modulation of magnon density at the resonant N-V-frequency via scattering between nonresonant MW-excited magnons and thermal magnons [21,29,31,32]. In this case, Γ is related to the oscillating ac magnetic field amplitude generated by resonant N-V- magnons, as described by $\Gamma \sim (\gamma_e/2)|B_\perp|^2$, with $|B_\perp|^2$ as the ac magnetic field component perpendicular to the N-V's quantum axis [14].

By assuming that the ac magnetic field from the resonant N-V- magnons evolves proportionally with the increase or decrease of magnetization precession of the MW-excited magnons [21] and based on the fact that magnetization precession evolves under a variation of ∇T [Eq. (1) and Figs. 3(f) and 3(i)], we can approximate an equation relating the longitudinal relaxation rate, Γ, and temperature gradient as [14,19,20,26]

$$\Gamma \propto \frac{\gamma_e^2}{2}\left|\frac{\lambda M_s \gamma_e b_{\mathrm{MW}}}{(\alpha_i + a\nabla T)\omega_r} k e^{-kx}\right|^2. \tag{2}$$

Data in Figs. 4(d) and 4(e) are fitted with Eq. (2), and α_{TM} is estimated to be $(4.3 \pm 1) \times 10^{-4}$ for $+B_{\mathrm{ext}}$ and $(2.5 \pm 0.9) \times 10^{-4}$ for $-B_{\mathrm{ext}}$; these results show good agreement with those estimated from the Rabi-oscillation experiments. We note that the temperature measurements at the middle of YIG, using a bulk diamond beam and infrared thermography (see Supplemental Material Note 4 and Note 5 [38]), confirm a base-temperature change of less than 1.5 K, which will give 0.7% of the change in Γ [21]. This change of Γ is small compared with the observed change of about 37.5% (for $+B_{\mathrm{ext}}$) and 23% (for $-B_{\mathrm{ext}}$) under applied ΔT from $+10$ K to -10 K to the YIG, showing that the observed effect is not due to the base-temperature change in the nanodiamond.

IV. DISCUSSION

We demonstrate the detection of thermally excited magnon currents mediated by MSSWs via N-V spins, where the thermal magnon spin-transfer torque emanating from the thermal magnon current alters the MSSW's magnetization precession when the YIG sample is subjected to a temperature gradient. Modulation of the magnetization dynamics of the MSSWs is perceived by the N-V spins as an alteration of the Rabi-oscillation frequency with resonant N-V spin excitation using a diamond beam.

Additionally, the longitudinal spin-relaxation rate change is observed with nonresonant N-V spin excitation using a nanodiamond. A possible explanation for the observed effect at nonresonant excitation may come from the four-magnon scattering process, where a magnon at microwave frequency scatters with a thermal magnon, resulting in two additional magnons, one of which possesses a frequency resonating at the N-V frequency [29,30]. The increase or decrease in the relaxation rate as a function of the temperature gradient indicates modulation of the population of the thermal magnon [Figs. 4(d) and 4(e)]. However, to determine a definite mechanism, it will require further experiments through changing excitation parameters and using a nanodiamond or diamond nanobeam with a well-defined N-V axis [21,39].

This study provides a detection tool for thermal magnon currents via N-V centers, which can be located locally and over a broad range of distances from spin waves. This feature cannot be obtained if only conventional methods, such as the ISHE, are used to investigate magnon dynamics, as conventional methods require a relatively large electrode and specific configurations with proximal distance to the spin waves. Owing to the N-V spin's single-spin detection sensitivity, enabled by its atomic scale size [51], nanoscale probing and imaging of thermal magnon dynamics can be realized in the future. For example, scanning-probe-based N-V magnetometry [13] will be useful for studying the nonuniformity of the thermal magnon current throughout the material at the nanoscale. Such measurements will be impractical through patterning a large area of a paramagnetic metal for ISHE measurements. A study of the thermal magnon dynamics with high spatial resolution can provide insights into practical applications in spin caloritronics and magnon spintronics [14,19,25].

ACKNOWLEDGMENTS

We thank E. Abe for fruitful discussions. This study is supported, in part, by JSPS KAKENHI (Grants No. 18H01868, No. 18H04289, and No. 19K15444), Japan; JST CREST (Grants No. JPMJCR1875 and No. JPMJCR17I1), and JST A-STEP (Grant No. JPMJTM 19AV), Japan. N.M. acknowledges support from KAKENHI (Grant No. 15H05868) and MEXT Q-LEAP (Grant No. JPMXS0118067395), Japan.

[1] A. V. Chumak, V. I. Vasyuchka, A. A. Serga, and B. Hillebrands, Magnon spintronics, Nat. Phys. **11**, 453 (2015).
[2] Y. Kajiwara, K. Harii, S. Takahashi, J. Ohe, K. Uchida, M. Mizuguchi, H. Umezawa, H. Kawai, K. Ando, K. Takanashi, S. Maekawa, and E. Saitoh, Transmission of electrical signals by spin-wave interconversion in a magnetic insulator, Nature **464**, 262 (2010).
[3] L. J. Cornelissen, J. Liu, R. A. Duine, J. B. Youssef, and B. J. van Wees, Long-distance transport of magnon spin information in a magnetic insulator at room temperature, Nat. Phys. **11**, 1022 (2015).
[4] B. L. Giles, Z. Yang, J. S. Jamison, and R. C. Myers, Long-range pure magnon spin diffusion observed in a nonlocal spin-seebeck geometry, Phys. Rev. B **92**, 224415 (2015).
[5] G. E. W. Bauer, E. Saitoh, and B. J. van Wees, Spin caloritronics, Nat. Mater. **11**, 391 (2012).
[6] L. J. Cornelissen, J. Liu, B. J. van Wees, and R. A. Duine, Spin-Current-Controlled Modulation of the Magnon Spin Conductance in a Three-Terminal Magnon Transistor, Phys. Rev. Lett. **120**, 097702 (2018).
[7] H. Wu, L. Huang, C. Fang, B. S. Yang, C. H. Wan, G. Q. Yu, J. F. Feng, H. X. Wei, and X. F. Han, Magnon Valve Effect Between Two Magnetic Insulators, Phys. Rev. Lett. **120**, 097205 (2018).
[8] K. Uchida, H. Adachi, T. Ota, H. Nakayama, S. Maekawa, and E. Saitoh, Observation of longitudinal spin-seebeck

effect in magnetic insulators, Appl. Phys. Lett. **97**, 172505 (2010).

[9] E. Saitoh, M. Ueda, H. Miyajima, and G. Tatara, Conversion of spin current into charge current at room temperature: Inverse spin-Hall effect, Appl. Phys. Lett. **88**, 182509 (2006).

[10] F. Casola, T. van der Sar, and A. Yacoby, Probing condensed matter physics with magnetometry based on nitrogen-vacancy centres in diamond, Nat. Rev. Mater. **3**, 17088 (2018).

[11] E. D. Herbschleb, H. Kato, Y. Maruyama, T. Danjo, T. Makino, S. Yamasaki, I. Ohki, K. Hayashi, H. Morishita, M. Fujiwara, and N. Mizuochi, Ultra-long coherence times amongst room-temperature solid-state spins, Nat. Commun. **10**, 3766 (2019).

[12] E. Abe and K. Sasaki, Tutorial: Magnetic resonance with nitrogen-vacancy centers in diamond—microwave engineering, materials science, and magnetometry, J. Appl. Phys. **123**, 161101 (2018).

[13] L. Thiel, Z. Wang, M. A. Tschudin, D. Rohner, I. Gutiérrez-Lezama, N. Ubrig, M. Gibertini, E. Giannini, A. F. Morpurgo, and P. Maletinsky, Probing magnetism in 2D materials at the nanoscale with single-spin microscopy, Science **364**, 973 (2019).

[14] T. van der Sar, F. Casola, R. Walsworth, and A. Yacoby, Nanometre-scale probing of spin waves using single electron spins, Nat. Commun. **6**, 7886 (2015).

[15] C. S. Wolfe, V. P. Bhallamudi, H. L. Wang, C. H. Du, S. Manuilov, R. M. Teeling-Smith, A. J. Berger, R. Adur, F. Y. Yang, and P. C. Hammel, Off-resonant manipulation of spins in diamond via precessing magnetization of a proximal ferromagnet, Phys. Rev. B **89**, 180406 (2014).

[16] C. S. Wolfe, S. A. Manuilov, C. M. Purser, R. Teeling-Smith, C. Dubs, P. C. Hammel, and V. P. Bhallamudi, Spatially resolved detection of complex ferromagnetic dynamics using optically detected nitrogen-vacancy spins, Appl. Phys. Lett. **108**, 232409 (2016).

[17] P. Andrich, C. F. de las Casas, X. Liu, H. L. Bretscher, J. R. Berman, F. J. Heremans, P. F. Nealey, and D. D. Awschalom, Long-range spin wave mediated control of defect qubits in nanodiamonds, Npj Quantum Inf. **3**, 28 (2017).

[18] D. Kikuchi, D. Prananto, K. Hayashi, A. Laraoui, N. Mizuochi, M. Hatano, E. Saitoh, Y. Kim, C. A. Meriles, and T. An, Long-distance excitation of nitrogen-vacancy centers in diamond via surface spin waves, Appl. Phys. Express **10**, 103004 (2017).

[19] T. X. Zhou, J. J. Carmiggelt, L. M. Gächter, I. Esterlis, D. Sels, R. J. Stöhr, C. Du, D. Fernandez, J. F. Rodriguez-Nieva, F. Büttner, E. Demler, and A. Yacoby, A magnon scattering platform, Proc. Natl. Acad. Sci. **118**, e2019473118 (2021).

[20] I. Bertelli, J. J. Carmiggelt, T. Yu, B. G. Simon, C. C. Pothoven, G. E. W. Bauer, Y. M. Blanter, J. Aarts, and T. van der Sar, Magnetic resonance imaging of spin-wave transport and interference in a magnetic insulator, Sci. Adv. **6**, eabd3556 (2020).

[21] C. Du, T. van der Sar, T. X. Zhou, P. Upadhyaya, F. Casola, H. Zhang, M. C. Onbasli, C. A. Ross, R. L. Walsworth, Y. Tserkovnyak, and A. Yacoby, Control and local measurement of the spin chemical potential in a magnetic insulator, Science **357**, 195 (2017).

[22] D. Labanowski, V. P. Bhallamudi, Q. Guo, C. M. Purser, B. A. McCullian, P. C. Hammel, and S. Salahuddin, Voltage-driven, local, and efficient excitation of nitrogen-vacancy centers in diamond, Sci. Adv. **4**, eaat6574 (2018).

[23] C. M. Purser, V. P. Bhallamudi, F. Guo, M. R. Page, Q. Guo, G. D. Fuchs, and P. C. Hammel, Spinwave detection by nitrogen-vacancy centers in diamond as a function of probe–sample separation, Appl. Phys. Lett. **116**, 202401 (2020).

[24] J. Liu, F. Feringa, B. Flebus, L. J. Cornelissen, J. C. Leutenantsmeyer, R. A. Duine, and B. J. van Wees, Microwave control of thermal magnon spin transport, Phys. Rev. B **99**, 054420 (2019).

[25] A. Solyom, Z. Flansberry, M. A. Tschudin, N. Leitao, M. Pioro-Ladrière, J. C. Sankey, and L. I. Childress, Probing a spin transfer controlled magnetic nanowire with a single nitrogen-vacancy spin in bulk diamond, Nano Lett. **18**, 6494 (2018).

[26] X. Wang, Y. Xiao, C. Liu, E. Lee-Wong, N. J. McLaughlin, H. Wang, M. Wu, H. Wang, E. E. Fullerton, and C. R. Du, Electrical control of coherent spin rotation of a single-spin qubit, Npj Quantum Inf. **6**, 78 (2020).

[27] H. Zhang, M. J. H. Ku, F. Casola, C. H. R. Du, T. van der Sar, M. C. Onbasli, C. A. Ross, Y. Tserkovnyak, A. Yacoby, and R. L. Walsworth, Spin-torque oscillation in a magnetic insulator probed by a single-spin sensor, Phys. Rev. B **102**, 024404 (2020).

[28] S. R. Etesami, L. Chotorlishvili, and J. Berakdar, Spectral characteristics of time resolved magnonic spin seebeck effect, Appl. Phys. Lett. **107**, 132402 (2015).

[29] B. A. McCullian, A. M. Thabt, B. A. Gray, A. L. Melendez, M. S. Wolf, V. L. Safonov, D. V. Pelekhov, V. P. Bhallamudi, M. R. Page, and P. C. Hammel, Broadband multi-magnon relaxometry using a quantum spin sensor for high frequency ferromagnetic dynamics sensing, Nat. Commun. **11**, 5229 (2020).

[30] H. Wang, S. Zhang, N. J. McLaughlin, B. Flebus, M. Huang, Y. Xiao, E. E. Fullerton, Y. Tserkovnyak, and C. R. Du, Quantum Sensing of Spin Transport Properties of an Antiferromagnetic Insulator, ArXiv:2011.03905 (2021).

[31] S. A. Bender and Y. Tserkovnyak, Thermally driven spin torques in layered magnetic insulators, Phys. Rev. B **93**, 064418 (2016).

[32] B. Flebus, P. Upadhyaya, R. A. Duine, and Y. Tserkovnyak, Local thermomagnonic torques in two-fluid spin dynamics, Phys. Rev. B **94**, 214428 (2016).

[33] L. Lu, Y. Sun, M. Jantz, and M. Wu, Control of Ferromagnetic Relaxation in Magnetic Thin Films Through Thermally Induced Interfacial Spin Transfer, Phys. Rev. Lett. **108**, 257202 (2012).

[34] Y. Kajiwara, K. Uchida, D. Kikuchi, T. An, Y. Fujikawa, and E. Saitoh, Spin-relaxation modulation and spin-pumping control by transverse spin-wave spin current in $Y_3Fe_5O_{12}$, Appl. Phys. Lett. **103**, 052404 (2013).

[35] M. B. Jungfleisch, T. An, K. Ando, Y. Kajiwara, K. Uchida, V. I. Vasyuchka, A. V. Chumak, A. A. Serga, E. Saitoh, and B. Hillebrands, Heat-induced damping modification in

yttrium iron garnet/platinum hetero-structures, Appl. Phys. Lett. **102**, 062417 (2013).

[36] H. Yu, S. D. Brechet, P. Che, F. A. Vetro, M. Collet, S. Tu, Y. G. Zhang, Y. Zhang, T. Stueckler, L. Wang, H. Cui, D. Wang, C. Zhao, P. Bortolotti, A. Anane, J.-P. Ansermet, and W. Zhao, Thermal spin torques in magnetic insulators, Phys. Rev. B **95**, 104432 (2017).

[37] J. R. Eshbach and R. W. Damon, Surface magnetostatic modes and surface spin waves, Phys. Rev. **118**, 1208 (1960).

[38] See the Supplemental Material at http://link.aps.org/supplemental/10.1103/PhysRevApplied.16.064058 for details of diamond-beam fabrication, measurement setups, temperature-gradient simulations and measurements, longitudinal spin-relaxation data, electrical measurements of spin-wave-resonance linewidths, derivation of equations, and data uncertainty. It includes Refs. [52–63].

[39] E. Lee-Wong, R. Xue, F. Ye, A. Kreisel, T. van der Sar, A. Yacoby, and C. R. Du, Nanoscale detection of magnon excitations with variable wavevectors through a quantum spin sensor, Nano Lett. **20**, 3284 (2020).

[40] V. M. Acosta, E. Bauch, M. P. Ledbetter, A. Waxman, L.-S. Bouchard, and D. Budker, Temperature Dependence of the Nitrogen-Vacancy Magnetic Resonance in Diamond, Phys. Rev. Lett. **104**, 070801 (2010).

[41] D. M. Toyli, D. J. Christle, A. Alkauskas, B. B. Buckley, C. G. Van de Walle, and D. D. Awschalom, Measurement and Control of Single Nitrogen-Vacancy Center Spins above 600K, Phys. Rev. X **2**, 031001 (2012).

[42] M. Fukami, C. G. Yale, P. Andrich, X. Liu, F. J. Heremans, P. F. Nealey, and D. D. Awschalom, All-Optical Cryogenic Thermometry Based on Nitrogen-Vacancy Centers in Nanodiamonds, Phys. Rev. Appl. **12**, 014042 (2019).

[43] C. Mühlherr, V. O. Shkolnikov, and G. Burkard, Magnetic resonance in defect spins mediated by spin waves, Phys. Rev. B **99**, 195413 (2019).

[44] A. Dréau, M. Lesik, L. Rondin, P. Spinicelli, O. Arcizet, J.-F. Roch, and V. Jacques, Avoiding power broadening in optically detected magnetic resonance of single NV defects for enhanced Dc magnetic field sensitivity, Phys. Rev. B **84**, 195204 (2011).

[45] P. Wang, Z. Yuan, P. Huang, X. Rong, M. Wang, X. Xu, C. Duan, C. Ju, F. Shi, and J. Du, High-resolution vector microwave magnetometry based on solid-state spins in diamond, Nat. Commun. **6**, 6631 (2015).

[46] P. Appel, M. Ganzhorn, E. Neu, and P. Maletinsky, Nanoscale microwave imaging with a single electron spin in diamond, New J. Phys. **17**, 112001 (2015).

[47] T. An, V. I. Vasyuchka, K. Uchida, A. V. Chumak, K. Yamaguchi, K. Harii, J. Ohe, M. B. Jungfleisch, Y. Kajiwara, H. Adachi, B. Hillebrands, S. Maekawa, and E. Saitoh, Unidirectional spin-wave heat conveyer, Nat. Mater. **12**, 549 (2013).

[48] K. L. Wong, L. Bi, M. Bao, Q. Wen, J. P. Chatelon, Y.-T. Lin, C. A. Ross, H. Zhang, and K. L. Wang, Unidirectional propagation of magnetostatic surface spin waves at a magnetic film surface, Appl. Phys. Lett. **105**, 232403 (2014).

[49] B. L. Giles, Z. Yang, J. S. Jamison, J. M. Gomez-Perez, S. Vélez, L. E. Hueso, F. Casanova, and R. C. Myers, Thermally driven long-range magnon spin currents in yttrium iron garnet due to intrinsic spin seebeck effect, Phys. Rev. B **96**, 180412 (2017).

[50] J. Shan, L. J. Cornelissen, J. Liu, J. B. Youssef, L. Liang, and B. J. van Wees, Criteria for accurate determination of the magnon relaxation length from the nonlocal spin seebeck effect, Phys. Rev. B **96**, 184427 (2017).

[51] J. Wrachtrup and A. Finkler, Single spin magnetic resonance, J. Magn. Reson. **269**, 225 (2016).

[52] J. F. Ziegler, M. D. Ziegler, and J. P. Biersack, SRIM – The stopping and range of ions in matter (2010), Nucl. Instrum. Methods Phys. Res., Sect. B **268**, 1818 (2010).

[53] D. M. Toyli, C. D. Weis, G. D. Fuchs, T. Schenkel, and D. D. Awschalom, Chip-scale nanofabrication of single spins and spin arrays in diamond, Nano Lett. **10**, 3168 (2010).

[54] J. Koike, D. M. Parkin, and T. E. Mitchell, Displacement threshold energy for Type IIa diamond, Appl. Phys. Lett. **60**, 1450 (1992).

[55] S. Sangtawesin, T. O. Brundage, Z. J. Atkins, and J. R. Petta, Highly tunable formation of nitrogen-vacancy centers via Ion implantation, Appl. Phys. Lett. **105**, 063107 (2014).

[56] S. Pezzagna, B. Naydenov, F. Jelezko, J. Wrachtrup, and J. Meijer, Creation efficiency of nitrogen-vacancy centres in diamond, New J. Phys. **12**, 065017 (2010).

[57] A. Prakash, B. Flebus, J. Brangham, F. Yang, Y. Tserkovnyak, and J. P. Heremans, Evidence for the role of the magnon energy relaxation length in the spin seebeck effect, Phys. Rev. B **97**, 020408 (2018).

[58] S. Kidalov and F. Shakhov, Thermal conductivity of diamond composites, Materials **2**, 2467 (2009).

[59] Y. A. Çengel and A. J. Ghajar, *Heat and Mass Transfer: Fundamentals & Applications*, 4th ed. (McGraw Hill Education, New York, NY, 2015).

[60] D. D. Stancil and A. Prabhakar, *Spin Waves* (Springer US, Boston, MA, 2009).

[61] S. D. Brechet and J.-P. Ansermet, Variational principle for magnetisation dynamics in a temperature gradient, EPL Europhys. Lett. **112**, 17006 (2015).

[62] F. D. Czeschka, L. Dreher, M. S. Brandt, M. Weiler, M. Althammer, I.-M. Imort, G. Reiss, A. Thomas, W. Schoch, W. Limmer, H. Huebl, R. Gross, and S. T. B. Goennenwein, Scaling Behavior of the Spin Pumping Effect in Ferromagnet-Platinum Bilayers, Phys. Rev. Lett. **107**, 046601 (2011).

[63] A. A. Serga, A. V. Chumak, and B. Hillebrands, YIG magnonics, J. Phys. Appl. Phys. **43**, 264002 (2010).